Development of nanowire single photon detectors based on hybrid superconducting materials

Cristina García Pérez

Máster en Nanociencia Molecular y Nanotecnología

MÁSTERES
DE LA UAM

2019 – 2020

Facultad de Ciencias

Universidad Autónoma
de Madrid

Master in

Molecular Nanoscience and Nanotechnology

Development of nanowire single photon detectors based on hybrid superconducting materials

Cristina García Pérez

Directors: **Daniel Granados Ruíz, Ramón Bernardo Gavito**
Tutor: **Amadeo López Vázquez de Parga**
IMDEA Nanociencia, Madrid, Spain

FACULTAD DE CIENCIAS

Master Thesis . Course 2019-2020

Universidad Autónoma de Madrid

Contents

List of Acronyms

- AFM – Atomic Force Microscopy
- APD - Avalanche Photodiode
- BSE – Back-scattered electrons
- CCD – Charge-coupled device
- CVD – Chemical Vapor Deposition
- DCR – Dark Count Rate
- DOS – Density of States
- EBICVD – Electron beam induced chemical vapor deposition
- EBID – Electron Beam Induced Deposition
- EBL - Electron Beam Lithography
- EDX – Energy-dispersive x-ray spectroscopy
- FEBID – Focused Electron Beam Induced Deposition
- FIBID – Focused Ion Beam Induced Deposition
- GIS – Gas Injection System
- HREELS – High-resolution electron energy loss spectroscopy
- HW-CVD – Hot wire CVD
- IBID – Ion Beam Induced Deposition
- LB-LMTO method – Linear orbital muffin tight-binding method
- LT – Low temperature
- NA – Numerical aperture
- PEs – Primary electrons
- PFEBID – Pulsed Focused Electron Beam Induced Deposition
- PMT - Photomultiplier tube
- PVD – Physical Vapor Deposition
- RAIRS – Reflection/absorption infrared spectroscopy
- RT – Room temperature
- SDE – System Detection Efficiency
- SEM – Scanning Electron Microscopy
- SEs – Secondary electrons
- SNR – Signal-to-noise ratio
- SNSPDs—Superconducting Nanowire Single-Photon Detectors
- SPADs - Single Photon Avalanche photodiodes
- SPD – Single-Photon Detector
- SSPD - Superconducting Single-Photon Detectors
- Tc – critical temperature
- TEM – Transmission Electron Microscopy
- UHV – Ultra-high vacuum
- VRH – Variable-range-hopping
- XPS – X-ray photoelectron spectroscopy

Acknowledgments

Abstract

A single-photon detector (SPD) is a device able to register events at the single quanta level. One type of SPD is the SNSPD (Superconducting Nanowire Single-Photon Detector). These are the ones under development in this master thesis. The key detection element in SNSPDs is a thin and long nanowire (approximately 100 nm wide or less), made of an ultrathin superconductor film (less than 100nm thick) and several microns long. They present unique and fast photoresponsive properties[1].

Conventional SPDs are commonly based on photomultiplier tubes (PMTs) or avalanche photodiodes (APDs)[1]. SNSPDs have overcome other traditional SPDs due to their numerous singular characteristics and advantages[2,3]. They show a lot of benefits for single-photon detection because of their high quantum efficiency[4] and their high sensitivity in a broad spectral range[4,5,6]. SNSPDs are promising for future quantum technologies [7]. Nevertheless, their operation is restricted to very low temperatures (T<2.4K) increasing their operation cost and complexity[1]. They have limitations related to the latching or reset time which originates from thermal conductance and kinetic inductance, which increases jitter and decreases operation bandwidth[8]. Their detection frequency band is also limited by the materials' superconducting bandgap.

To overcome these limitations, we propose a new approach based on the fabrication of hybrid systems based on tungsten carbide (WC) and graphene. This works aims to demonstrate how we can take control over not only the geometry but also the composition of the WC nanowires with nanofabrication techniques. The nanowires are produced via Pulsed Focused Electron Beam Induced Deposition (PFEBID) onto SiO_x/Si substrates. To our knowledge, this is the first time this fabrication scheme has been employed for the development of similar practical devices[9].

The main objective of this project is to characterize them by Scanning Electron Microscopy (SEM), Atomic Force Microscopy (AFM), micro-Raman spectroscopy, electrical IV measurements (two-probe method), and reflectance images. Here, we report our preliminary results based on these experimental measurements. We have fabricated nanowires with a high aspect-ratio. The experimental results obtained by Raman spectroscopy show peaks corresponding to amorphous carbon in the region of tungsten carbide deposits. The resistivity values vary from $1.15 \cdot 10^8$ $\Omega \cdot$cm to $3 \cdot 10^9$ $\Omega \cdot$cm depending on the deposition parameters, indicating there is probably a low tungsten content.

We hope this work contributes to establishing growth protocols using Focused Electron Beam Induced Deposition (FEBID) that results in superconducting materials with a sharp transition into the superconducting state and reproducible properties. We expect that our research will contribute to the development of quantum technologies, for example, for its use as a single-photon detector in quantum key distribution experiments.

Resumen

Un detector de fotones individuales (SPD) es un dispositivo capaz de registrar eventos a nivel de un único cuanto de energía. Un tipo de SPD es SNSPD (Superconducting Nanowire Single-Photon Detector). Estos son los que se encuentran en desarrollo de esta tesis de máster. El elemento clave de detección en SNSPDs es un nanohilo largo y estrecho (de aproximadamente 100 nm de anchura o menos), fabricado a partir de una lámina superconductora ultrafina (menos de 100 nm de espesor) y de varias micras de longitud. Presentan propiedades de fotorrespuesta rápidas y únicas[1].

Los SPDs convencionales están basados comúmente en tubos fotomultiplicadores (PMTs) o fotodiodos de avalancha (APDs)[1]. Los SNSPDs han superado a otros SPDs tradicionales debido a sus numerosas y singulares características y ventajas[2,3]. Presentan numerosos beneficios para la detección de fotones individuales debido a su elevada eficiencia cuántica[4] y su elevada sensibilidad sobre un amplio rango espectral[4,5,6]. Los SNSPDs son prometedores para las futuras tecnologías cuánticas[7]. Sin embargo, su operación está restringida a temperaturas muy bajas (T<2.4K) aumentado su complejidad y coste de operación[1]. Muestran limitaciones relacionadas con el latching o reset time que se origina a partir de la conductancia térmica e inductancia cinética, lo cual aumenta el jitter y disminuye el ancho de banda de operación[8]. Su banda de frecuencia de detección está también limitada por el bandgap superconductor.

Para superar estas limitaciones, proponemos una nueva aproximación basada en la fabricación de sistemas híbridos basados en carburo de tungsteno (WC) y grafeno. Este trabajo tiene como objetivo demostrar cómo podemos controlar no solo la geometría sino también la composición de nanohilos de WC mediante técnicas de nanofabricación. Los nanohilos son fabricados mediante Pulsed Focused Electron Beam Induced Deposition (PFEBID) sobre sustratos de SiO$_x$/Si. Para nuestro conocimiento, esta es la primera vez que este tipo de fabricación se emplea para el desarrollo de dispositivos prácticos similares[9].

El principal objetivo de este projecto es caracterizarlos mediante microscopía electrónica de barrido (SEM), microscopía de fuerza atómica (AFM), espectroscopía micro-Raman, medidas eléctricas IV (método de 2 puntas) e imágenes de reflectancia. Aquí, mostramos nuestros resultados preliminares basados en medidas experimentales. Hemos fabricado nanohilos con un elevado aspect-ratio. Los resultados experimentales obtenidos mediante espectroscopía Raman muestran picos que se corresponden con carbono amorfo en la región de los depósitos de carburo de tungsteno. Los valores de resistividad varían desde $1,15.10^8\,\Omega$·cm hasta $3.10^9\,\Omega$·cm dependiendo de los parámetros de depósito, indicando que probablemente hay un bajo contenido de tungsteno.

Esperamos que este trabajo contribuya al establecimiento de protocolos de crecimiento utilizando técnicas de depósito inducido por haz de electrones focalizado (FEBID) que resulte en materiales superconductores con una pronunciada transición superconductora y propiedades reproducibles. Esperamos que nuestro trabajo contribuya al desarrollo futuro de tecnologías cuánticas, por ejemplo, su utilización como detectores de fotones individuales en experimentos de distribución de claves cuánticas.

1. Background and theory

This chapter reviews the state-of-the-art of superconducting nanowire single-photon detectors, some photodetectors terminology, their mechanism of photodetection, as well as an introduction to superconductivity and properties of tungsten carbide.

1.1 Single Nanowires Single-Photon Detectors (SNSPDs)

The photodetection phenomenon consists of the conversion of the light absorbed into a measurable signal[10]. One of the contributions of Einstein to modern physics was the affirmation that light was composed of individual packets of energy which are known as photons[1]. In particular, a single-photon detector (SPD) is a device that can register these quantum objects one by one[1].

In 1996, Kadin et al. proved that superconducting devices could be employed to develop SPDs. By solving the heat flux equation, it was predicted that a path to develop SPDs would be possible if a superconducting film with a size in the nanoscale was used[11]. This turned into reality with a nanowire of NbN at T=4.2 K in the year 2001[11]. The interest in these detectors has increased over the last few years[1]. Moreover, it is expected it continues increasing because of the intention in improving the security as well as their potential applications in quantum optics[12].

There are several types of SPDs such as photomultiplier tubes (PMTs) or single-photon avalanche photodiodes (SPADs)[1]. PMTs can detect single photons but with low efficiencies in the visible and in the telecommunications band where communication technology and quantum information are being developed[13]. Silicon APDs and many PMTs are insensitive to $\lambda > 1\mu m$[14]. In the IR range, some InGaAs or Ge APDs may have reasonable detection efficiencies but suffer from afterpulsing and high DCR[14]. These terms are introduced below.

1.1.1 Photodetectors terminology

Some specific terms, which are very common in detectors research, are introduced in the following table:

Table 1. Photodetectors terminology definition

Recovery time or detector dead time (τ or t_D)	The time interval after the absorption of a photon when the detector is unable to record another photon reliably[1,5,6,11] .This limits the maximum rate of photons that can be measured[5].
Timing jitter	The temporal resolution of a detector. It measures the uncertainty or fluctuation in the delay time between the absorption of a photon and the instant at which a photodetection pulse is recorded[6].
Dark Count Rate (DCR)	The rate of the response pulse that is not due to signals from the incident photons. It depends on factors such as the superconducting material readout mechanism, electronics or the experimental set-up[6].
Detection Efficiency or System Detection Efficiency (SDE)	The probability of detecting a signal produced by a photon once it has entered the aperture of the detection system[6].
Afterpulsing	The generation of several electrical pulses for each single photon detected[6].
Sensitivity	Relative efficiency of detection of a signal, as a function of its frequency[15].

1.1.2 State-of-the-art

Before exploring the state of the art of single-photon detectors, we must review what superconductivity consists of. Superconductivity means that for a metallic material there is no electrical resistance below a critical temperature, electrical current, or magnetic field. If the temperature, electric current, or magnetic field exceeds a critical value the superconductivity state is lost and a state of finite electrical resistance appears. According to the BCS theory in honor to John Bardeen, Leon Cooper, and John Robert Schrieffer[16], the origin of superconductivity is the interaction between the electrons mediated by the phonons in a solid.

In a superconducting state, charge carriers are formed by coupled pairs of electrons called Cooper pairs. They are pairs of electrons that experience an attraction potential larger than the Coulomb repulsion, which is mediated by the phonons in the solid[16]. This attraction is possible because the electrons in the metals go very fast (at $v_F \sim 10^{16} \dot{A}s^{-1}$), this speed is huge and the relaxation time of the lattice is so low ($\omega_{lattice\ relaxation} \sim 10^{-13}s^{-1}$) therefore the electrons coming behind see the lattice strained and they can interact with the phonons. In this way, a Cooper pair is created, as a bound state between two electrons exchanging a phonon. In the superconducting state a forbidden energy gap opens, known as the superconducting gap. The energy E required to break a cooper pair is $E = 2 \triangle_0$, being $\triangle_0 \approx 1.76 k_B T_c$.

One type of superconducting detector is SNSPD, whose mechanism of photodetection is described in section 1.3. In them, the photodetector element is a nanowire with a width of approximately 100 nm that is obtained from a superconducting sheet with a thickness of 5 nm[1,5]. One of the advantages over other detectors is its sensitivity over a high spectral range, as well as a low DCR and low jitter[4,5,6]. The materials used for this type of detectors are NbN, $NbTiN$, MgB_2, YBa_2Cu_3O, $MoGe$, $MoSi$, Nb and W_xSi_{1-x}[17,18]. The first two have been used due to their high Tc and Jc[18]. NbN has been used as the material of choice due to the possibility of being able to be deposited on a sheet with a thickness of around 4 nm[19]. However, these deposits have limitations such as the need to grow on substrates with lattice coupling[1] or that they are very sensitive to external conditions and can oxidize and degrade the performance of the detector[20]. An interesting approach is to manufacture devices with tunable composition. For example, it has been seen that pure W has a critical temperature $(Tc) \sim 15$ mK[17] but in sheets with tunable composition, an increase in by more than two orders of magnitude has been observed[17]. Likewise, other amorphous sheets such as $Mo_{0.75}Ge_{0.25}$ present Tc around 5 K[18].

1.2 Properties of tungsten carbide (WC)

Due to the physical and chemical properties of carbides, such as their extreme hardness, high melting point, and chemical stability[21], they have attracted interest in the electronics industry. Tungsten carbides exist in different phases, being WC the most stable of them[21]. Concerning its electrical properties, both the density of electronic states (DOS) and its electronic band structure confirm its metallic nature[21]. Therefore, there is no gap between the bands. However, the bond between W and C is not only metallic but is also comprised of covalent contributions due to hybridization between W and C atoms as well as ionic contributions due to charge transfer between them[21].

Regarding its superconducting properties, it has been seen that Tc depends on the material crystallographic phase[22]. In this theoretical study[21] using the linear orbital muffin tight-binding

method (LB-LMTO method) the computed value for WC Tc was 9.23 K[21]. Growing technique influences superconducting properties, as will be discussed in later sections. In nanowires with lateral width and thickness ~ 200 nm, the Tc was approx 5.1 K[23] and in ultra-narrow W nanowires the Tc was between 4.2 and 4.8 K[23]. As mentioned in the previous section, while in pure and crystalline W it has a Tc = 0.01 K in nanodeposits of W of an amorphous nature and whose composition was W: 40% at, C = 40% at, and Ga = 20% at, they showed a Tc of approx 5.2 K[23]. Besides, it has been observed that amorphous films of W by different techniques have a similar Tc[23].

1.3 Mechanism of photodetection in SNSPDs

The photodetection mechanism in SNSPDs devices consists of a combination of the superconducting properties, which depend on the material, but also on the width, length, thickness, and geometry of the wire [24]. As can be seen in *Figure 1*, when a photon hits the active region of the detector, the absorption of this photon breaks the Cooper pairs forming a "hot-spot" where the superconducting gap is suppressed[18]. This induces a transition in the nanowire from a superconducting state to a resistive state[6,25]. For this to be possible, the thickness of the nanowire must be comparable to the size of the hot spot that originated after the absorption of the photon[18]. The hot-spot produces a voltage pulse along the transmission line[25]. Finally, the current is diverted from the nanowire towards the reading electronics, which allows it to dissipate the energy provided by the absorbed photon and return to the initial superconducting state to be able to detect another photon[4,6,24].
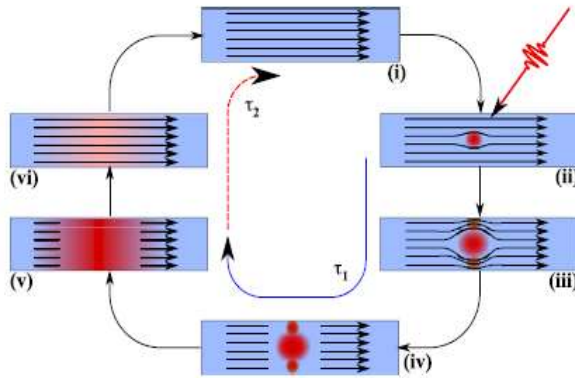
Figure 1. Extracted from (11). Detection cycle.

(i) Nanowire in its superconducting state

(ii) A small hot-spot is created after the absorption of an individual photon.

(iii) The current around the hot-spot increases overcoming the critical value.

(iv) The superconductivity disappears. A resistive region appears across it section and (v) grows by Joule heating.

(vi) Decrease of the resistive region and recovery of the superconducting state.

2. Experimental methods

In this chapter, the experimental fabrication and characterization techniques along with the instrumentation used are described.

2.1 Device fabrication

Firstly, we explain the fabrication technique used to fabricate our devices.

2.1.1 Pulsed Focused Electron Beam Induced Deposition (PFEBID)

The diffusion of boundaries between physics, chemistry, and biology makes the need for a manufacturing technique that is simultaneously accessible, versatile, and flexible[26]. Controlling the matter at the nanoscale by fabricating artificial structures can lead to new properties[27]. Previously, WC nanostructures have been manufactured using different methods such as traditional carbothermal synthesis[28], sputtering[29], hot wire chemical vapor deposition (HW-CVD) using a W and CF_4 filament[30] or decomposition of tungsten hexacarbonyl 600-800 °C[28]. In particular, using a focused ion or electron beam has attracted significant interest because of the ability to deposit material with high spatial precision[31,32]. It provides an excellent tool for nanotechnological applications[31,32].

As it is a direct manufacturing technique unlike other lithography techniques, process steps are saved. A novel approach to fabricate nanomaterials is Focused Electron Beam Induced Deposition (FEBID)[27]. This is a one-step technique used to prepare nanostructures in one, two, or three dimensions[23,27]. FEBID is a direct-write lithographic technique whose lateral resolution competes with advanced electron lithography[33,34]. For instance, the resolution of state-of-art of electron beam lithography (EBL) reaches a resolution between can reach approximately 3 - 5nm[23,35]. FEBID has also a nanometric resolution but it has the advantage of avoiding all the steps of the lithography process. This resolution is of great interest for the fabrication of superconducting nanowires[33]. It is important to highlight the role of the surface-to-volume ratio on the superconductor's phase boundaries[33]. On one hand, for bulk samples are determined by the material itself as a consequence of the very small surface-to-volume ratio[33]. On the other hand, in nanostructures this ratio is large and the shape imposes specific boundary conditions playing a fundamental role in controlling the spatial development of the superconducting state[33]. Another advantage of FEBID is the possibility it offers to fabricate suspended structures singly and simply, without a substrate to support them.

It has been suggested that this technique has the potential to become not only the basis of electron beam controlled technology but also the control of chemistry at the nanoscale[32]. The observation of the deposition of individual organic molecules[35] and its high resolution has placed this technique in the same spatial regime as bottom-up chemistry[35]. It provides a tool for electron-controlled chemistry in a nanometric space regime[32]. Despite this, the development of surface chemistry using this method is still in its infancy[32]. FEBID uses the molecular decomposition induced by electrons[34]. It can be considered as chemical vapor deposition (CVD) assisted by a focused electron beam[23]. It serves both to deposit and to etch materials[36]. The process involves the introduction of a precursor gas that contains the desired material into the vacuum chamber inside of an electron microscope[31,32,35] or dual-beam[23,26]. A gas injection system (GIS) injects the precursor gas directed to the substrate through a nozzle that is close to the focused beam and it is adsorbed onto the sample's surface[31,34]. This molecular precursor adsorbed on the surface is dissociated by a highly energetic focused electron beam (1-200 keV)[34] that breaks the molecules losing of carbonyl

ligands in metal carbonyl coordinated compounds[26]. By varying the distance between the nozzle and the sample it is possible to control the effective flow of precursor reaching the surface of the sample of interest[26,32].

Figure 2 shows a set-up for this technique. The electron beam is scanned on the surface of the sample to generate the desired pattern, using a pattern generator[27,31,32]. This beam settles on each point for a determined dwell-time[33]. Dwell-time is the total time in which each particular position is irradiated by the electron beam during which it remains constant[26,32]. After completing the irradiation following the desired pattern, the process is repeated over a predefined number of loops[32,33].
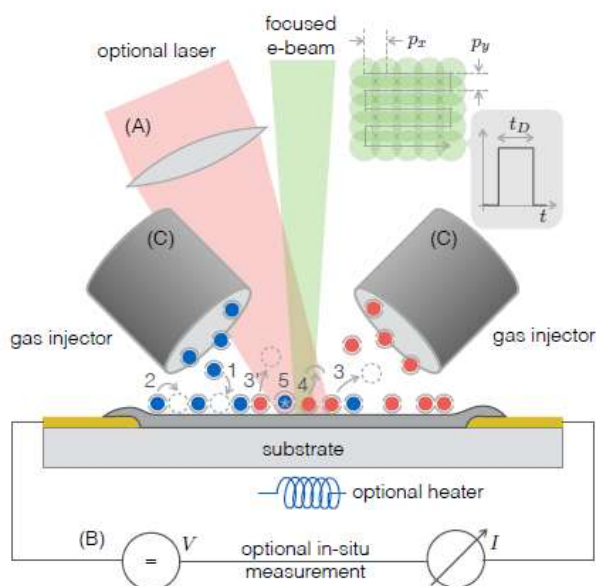

Figure 2. Set-up system for Focus Electron Beam Induced Processing. Extracted from (33).

(A) Pulsed IR-laser
(B) In-situ electrical characterization
(C) Gas injection channels

(1) Physisorption
(2) Diffussion
(3) and (3') Desorption
(4) Dissociation and desorption

The residence time of the precursor is different on the substrate than on the material already deposited[32]. The precursor gas is decomposed into volatile and non-volatile components[27,31,34]. The last leave a residue known as a deposit[26,27,34]. This deposit grows at an interaction point between the incident beam and the substrate[34]. The volatile fragments must be desorbed to avoid being included into the deposit[26,35]. The deposition is a complex process where electrons, the sample, the adsorbed precursor, and the surrounding atmosphere come into play[36].

In the same way as any chemical reaction, this process is characterized by a reaction rate[36]. As the surface influences opening or modifying reaction channels, this process becomes more complex[36]. During electron irradiation, the highly energetic primary electrons (PEs), when interacting with the substrate, generate low energy secondary electrons (SEs) (<500 eV) and back-scattered electrons (BSE)[23,36] and there is an equilibrium between them[26,34].

SEs are produced as a result of inelastic collisions with outer shell electrons[32]. As a consequence, the deposited material is irradiated continuously during the writing process[32] and electrons are generated on a surface that is continuously modified during the deposition process[23]. In the absence of aberrations, the radial distribution flux of electrons on the surface has a Gaussian shape[23,32] and the spectrum of the secondary electrons depends on the properties of the substrate[32]. The shape and size of the interaction region under the beam depends on the angle of incidence and the acceleration voltage of the beam, as well as on the nature of the substrate[23]. The resolution of this technique is determined by the diameter of the electron beam in the convoluted focal area with

the secondary electrons (SEs) leaving the surface[32]. The writing process is governed by parameters such as the energy of the primary beam, the beam current, the dwell time, the pitch or the distance between nearby dwell points, the number of loops, or the time in which the writing pauses between two successive loops known as replenishment time (t_r)[23,32]. The novelty of our technique and that's the reason why it receives the name of pulsed is that we stop the beam current when we finish fabricating a line of nanowire for 50 ms. As a consequence, there is always a precursor available that reaches the surface.

Although it has been seen that the integral metal content is usually higher using ions than using electrons by employing the same precursor[33], it is generally preferred to use electron-induced deposition over ion-induced deposition because ion contamination, etching or induction of redeposition of material in an undesired way are avoided[34]. Despite this, one of the main limitations of the technique that uses electrons is the control of the purity of the final product[36].

More specifically, metallic nanostructures manufactured using organometallic precursors have levels of organic contamination, mainly carbon or oxygen that affect their properties[34]. However, if process conditions for maximum metal content are used it results in metallic deposits[33], as it has been possible using precursors such as $Co_2(CO)_8$ or $Fe(CO)_5$[32].

In this project, the nanowires have been fabricated by PFEBID in a Carl-Zeiss SEM microscope (Auriga Cross Beam) inside a class 100/1000 cleanroom. We have used a $W(CO)_6$ precursor. As in similar works by other research groups, the electron beam was controlled via a Raith Lithography system[31]. The deposition parameters we selected were 2.5 keV and a beam current of 0-2-0.22nA. The electron dose was between 220 $\mu C/cm^2$ and 4.10^6 $\mu C/cm^2$ depending on the dwell time (between 0.1 ms and 0.001 ms) and the number of loops (between 1 and 2000). Some samples of nanowires were grown onto SiO_x / Si substrate, with a thickness of 285 nm/525 μm and without pre-patterned electrodes. Other samples were grown onto similar substrates with pre-patterned electrodes made of Cr/Au, with a thickness of 10/70 nm. The metal electrodes have been fabricated using UV lithography, subsequent metal evaporation and lift-off[27,31].

2.1.2 Decomposition of the precursor

The nature of the precursor influences the process of its decomposition under the beam[23]. The precursor we have used is tungsten hexacarbonyl ($W(CO)_6$). It has been anticipated that this precursor does not decompose in W[35] since under electron irradiation organometallic compounds rarely decompose into pure metallic species[23,35]. It has been speculated that secondary reactions between volatile fragments of precursors could give rise to less volatile organic species that could be included in the deposits[32]. The resulting material consists of precursor ligands that have not been removed by electrons[35]. To obtain details of the dissociation process, the structure of the chemical bond is highly relevant[32].

Generally, when organometallic precursors are used, structures with low metallic content are obtained[35]. Some studies have affirmed that after the adsorption of $W(CO)_6$, the initial step is the desorption of multiple carbon monoxide ligands[34,37] so partially decarbonylated tungsten species are formed[37]. Afterward, as can be seen in **Figure 3**, these species lead to ligand decomposition producing oxidized tungsten that is incorporated in a carbonaceous matrix[37]. Moreover, SEs seem to be responsible for these reactions[23,37]. These can induce not only the dissociation of precursor molecules but also of polluting species in the environment[23] as hydrocarbons introduced by

lubricant oil, vacuum grease, or photoresist, that are present for instance in silicone oil or polyepoxides[38]. However, contributions from high-energy electrons[23] cannot be excluded.
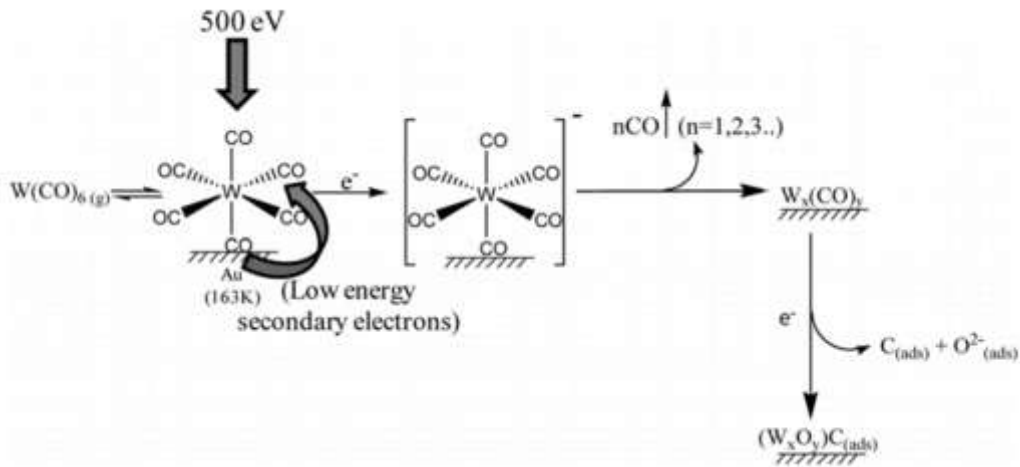

Figure 3. The decomposition process of W(CO)$_6$ on a surface. Extracted from (37).

2.2 Characterization techniques

In the section of this chapter, morphology aspects are analyzed with atomic force microscopy (AFM) and scanning electron microscopy (SEM). The compositional analysis will be carried out by Raman spectroscopy and electrical properties by two-probe electrical IV measurements in a probe station at room temperature (RT).

2.2.1 Atomic Force Microscopy and Scanning Electron Microscopy

The scanning probe methods can create 3D images of surfaces with nanometric resolution. One type is Atomic Force Microscopy (AFM) in which the magnitude of the force between the tip and the surface atoms of the sample is monitored[39,40,41]. This is a probe microscopy technique with very high resolution which does not require either an expensive and energetic source of radiation or vacuum chambers or complex installations. In AFM a tip is held under a cantilever whose mechanical deflection is used to obtain information about the topography of a surface. The short-range forces between the atoms of the sharp tip and the sample cause the deflection of the cantilever. It is based on a balance between attractive Van der Waals-like forces and electrostatic repulsive forces between the tip and the surfaces and the relation between the cantilever and the applied force is described by the Hooke's law[39,40,41]. This is based on the deviation of the optical signal from the laser on the top surface of the cantilever by the mechanical deflection into a photodiode[40,41]. The resolution depends on the curvature radius and the sharpness of the tip, the surface geometry of the sample, and the scanning mode[42]. The typical resolution in XY is around 10 nm and below 1 nm in Z. We have carried out these measurements in contact mode. As in this method, the tip is continuously touching the sample, it is riskier than other scanning modes. However, if the samples are nearly plane, this problem is avoided and it usually provides topographic images with a better spatial resolution[39]. Moreover, samples with hard surfaces such as tungsten carbide are appropriated for AFM analysis in contact mode[40].

In this project, the thickness measurements of the WC nanowires were performed using an NT-MDT NTegra Prima AFM[43] with a 100 μm scanner and a universal head where the cantilever, the laser, the photodiode, and the sensor are located[42]. To cancel the external vibrations, the microscope

is on top of a vibration isolation table[42]. We have used HA_CNC high accuracy contact composite probe with a silicon body, polysilicon lever, and silicon tip from NT-MDT[42,44]. The cantilever length was 224 ± 2 μm and the force constant was $1.0 \pm 20\%$ N/m. The total tip height was 9 to 16 μm and the tip curvature radius was <10 nm.

As the measurement of the width of the nanowires by AFM depends on the tip, we have also determined it by SEM. This is an electron probe method where a high energy electron beam is originated from an electron gun and accelerated by a set of collimators and magnetic lenses. The electrons' interactions and the secondary effects of these interactions are detected and transformed into images [40,45].

2.2.2 Micro-Raman spectroscopy

When light interacts with matter the main part of scattered light does not change its energy (Rayleigh scattering) However, a little part of the incident photons is scattered towards frequencies different from the frequency of the incident light[46]. Raman Spectroscopy is based on the Raman effect that is a scattering phenomenon based on the inelastic interactions of photons with the vibrational modes of a sample. The scattered photons can gain or lose energy. Stokes lines are generated when these frequencies are lower than the excitation frequency of the Raman laser. The opposite happens in anti-Stokes scattering[42,46].
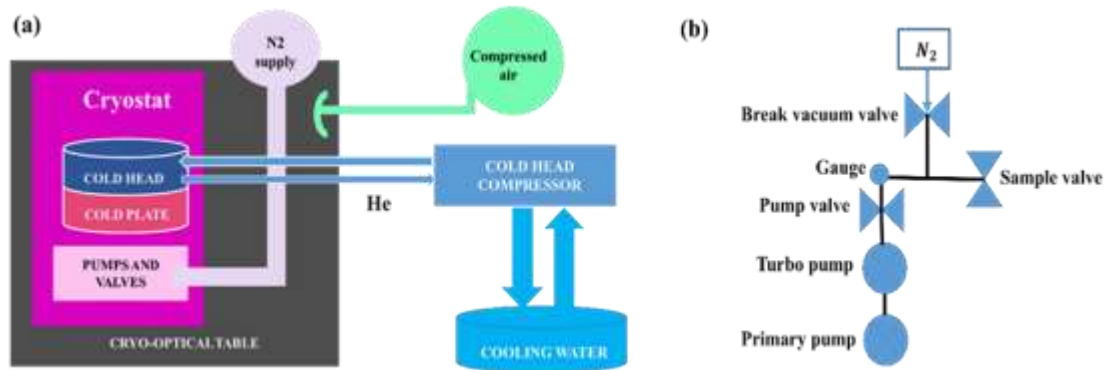
Figure 4. (a) Structure of the system. Adapted from (47). Compressed air is connected to pneumatic vibration isolators of the cryo-optical table. The cold head compressor, cooled by water, provides helium to the cryostat set-up. It contains the pumps and valves, cold head, and cold plate. (b) Vacuum diagram system extracted from (47). It consists of a turbo and a primary pump, two valves, and a nitrogen supply.

Our experimental set-up is comprised of attoDRY800 system including a closed-cycle cryostat integrated into an ultra-low vibration optical table positioned on the floor with pneumatic isolators to minimize mechanical disturbances. The vibration level is lower than 5 nm[47]. The temperature range of the system varies between 3.8 and 320 K and the temperature stability is lower than 10 mK. The base pressure in the sample chamber is $\sim 1.10^{-6}$ mbar[47].The motion of the sample is carried out by a set of positioners and scanners. They are controlled by piezo motion controller ANC-350[48] and piezo positioning electronic ANC300[49]. The linear z-, x-, and y-nanopositioners have a travel range of 5 mm, 6 mm, and 6 mm, respectively. The fine linear positioning range is 5 μm at RT[47-50]. The sample is placed on a stack of positioners and it is connected to the positioner adapter by a thermal link.

There is also an optics holder positioning in which is mounted the objective LT-APO/VIS/0.82 with a clear aperture of 4.7 mm, a focal length of 2.87 mm, a numerical aperture (NA) of 0.82, and a working distance of 0.65 mm. The range travel at RT of the scanner XY is 50x50 μm whereas the scanner z is 24 μm[47-50]. The cryostat has vacuum pumps, a cold plate, and control electronics. A helium compressor cools the cold head and the cold plate in which is mounted the sample (**Figure 4**(a)). It includes the thermal shield, the vacuum shroud, and positioning arrangements[47,50]. The pumps and valves arrangement (**Figure 4**(b)) consists of a primary membrane pump, a turbo-molecular pump, a pressure gauge, and three valves (pump valve, sample valve, and break vacuum valve). The break vacuum valve is used for venting the system with nitrogen to flush the vacuum chamber during sample exchange[47].
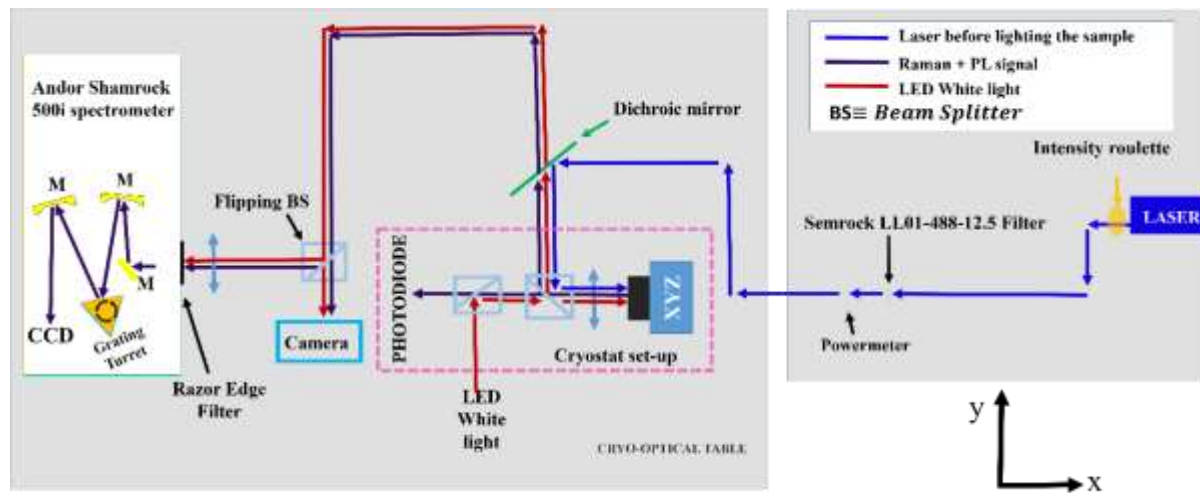

Figure 5. Micro-Raman optical set-up. Consists of a 488 nm laser source, a set of mirrors and beam splitters to guide the beam, a 488 nm line filter, a dichroic mirror, a white LED, an objective to focus on the sample located on the XYZ piezo stage, a photodiode, a camera, a razor edge filter and an Andor Shamrock 500i spectrometer. Inside the spectrometer there is a grating turret and a CCD.

This research was performed at RT with an optical set-up (**Figure 5**) with a 488 nm wavelength argon-ion laser at 1 mW power. Several mirrors are used to control the beam direction. A roulette which regulates the intensity and output power light of excitation. Firstly, the laser beam passes through a line filter which selects the 488 nm wavelength blocking light with different frequency. The laser beam passes through a Semrock LL01-488-12.5 line filter which blocks all non-laser signals. The laser beam is guided following the optical path and it finally reaches a dichroic filter[42,51]. After that, it enters inside a covered region to block ambient light, and after passing through a beam splitter enters into the cryostat set-up.

White light provided by a LED follows the same optical path of the laser beam until it reaches a 90° flipping beam splitter near a camera. In this system, we can simultaneously look at the sample and the laser spot[42]. The laser beam passes through a Semrock LL01-488-12.5 Filter and a Dichroic mirror. When the laser enters into the cryostat set-up, goes through the objective that focuses the beam in the perpendicular direction to the surface sample to analyze[42]. On the top part of this system, there is a photodiode that receives the light reflected from the sample after being illuminated by the laser beam. Both Raman signal plus LED white light go out of the cryostat system and returns to the dichroic filter which has a cut-off at 488 nm when the beam is

transmitted[42,51]. The Raman signal finally passes through a lens and razor edge filter[52] to enter into the spectrometer. This contains a rotating turret. There are three different diffraction gratings with different groove spacing. As a consequence, the angle of the diffracted light will be different so the bandwidth varies[42].

In this case, the measurements were carried out with the Grating 2 with a bandwidth of 169 nm and 300 lines starting from 488 nm. Translating this into Raman shift (cm^{-1}) the wavenumber range spans from 0 to 5271 cm^{-1}.[42]

Finally, the diffracted light is guided by a set of internal mirrors to a charged-couple device (CCD) camera that converts the optical signal into an electrical signal. This signal is processed by the Andor Solis software and give us counts of intensity[42]. Data treatment is performed in R scripts that I have programmed using Rstudio. This script gives a video which provides information about the regions of the sample that are more or less emissive at different Raman shift with the spatial resolution because we can correlate the optical image of the camera together with the reflectivity map and the micro-Raman mapping. Several coordinates in the (XY) plane help us to identify regions to extract spectra with high spatial precision.

2.2.3 Electrical characterization

Two-probe electrical measurements have been performed at RT in a probe station (**Figure 6**) over the samples corresponding to nanowires over SiO_x/Si substrates and Cr/Au electrodes. For the measurements, a Keithley 4200-SCS was used to apply a bias voltage between a different range.
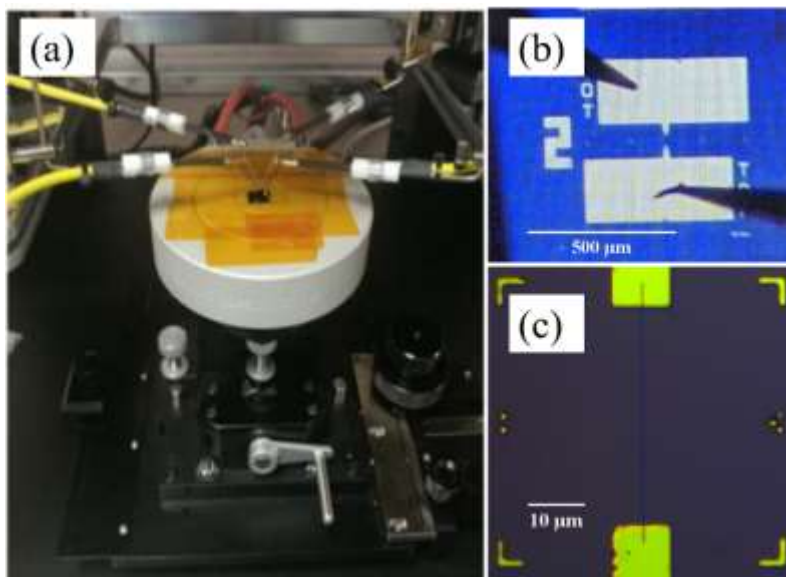

Figure 6.

(a)Probe Station set-up. Zoom of the XYZ stage. Extracted from (53)

(b)Probes contacting electrode pads.

(c)Optical microscopy image of a nanowire.

3. Results and discussion

In this chapter, we present a list of the samples fabricated and their deposition parameters. In the following sections morphology, composition, and electrical properties will be discussed.

3.1 Sample list

In Table 2 there is the sample list with the deposition parameters. Samples A_0, A_1, B_0 and B_{2D} are used to study their electrical properties. The first three ones only differ in their length and/or the number of nanowires. The sample B_{2D} has been fabricated with the same length and beam current than B_0, but they have a different number of nanowires as well as a different number of loops, dwell-time, step size and line spacing. The samples from AFM#1 to AFM#2000 are arrays of 4 nanowires 1 µm length used to study their morphology by AFM technique. They differ from each other just in the number of loops. The samples Square#20 and Square#50 are used to study their composition by Raman spectroscopy. They have been fabricated with the same deposition parameters than the AFM samples but instead an array of 4 nanowires they consist of an array of 4 squares, with 20 and 50 loops, respectively. The dose is charge per unit area and its formula is: $Dose = Loops \cdot Beam\ current \cdot Dwell\ time$.

Table 2. Sample list with deposition parameters.

NAME	Description	Length (µm)	Beam current (nA)	Loops	Dwell time (ms)	Dose (µC/cm²)	Step size (nm)	Line spacing (nm)
A_0	5 nanowires	15	0.2	50	0.1	$4 \cdot 10^6$	5	5
A_1	1 nanowire	20	0.2	50	0.1	$4 \cdot 10^6$	5	5
B_0	1 nanowire	25	0.2	50	0.1	$4 \cdot 10^6$	5	5
B_{2D}	5 nanowires	25	0.2	2500	0.001	$5.5 \cdot 10^5$	10	10
AFM#1	4 nanowires	1	0.22	1	0.001	220	10	10
AFM#5	4 nanowires	1	0.22	5	0.001	$1.1 \cdot 10^3$	10	10
AFM#10	4 nanowires	1	0.22	10	0.001	$2.2 \cdot 10^3$	10	10
AFM#20	4 nanowires	1	0.22	20	0.001	$4.4 \cdot 10^3$	10	10
AFM#30	4 nanowires	1	0.22	30	0.001	$6.6 \cdot 10^3$	10	10
AFM#700	4 nanowires	1	0.22	700	0.001	$1.54 \cdot 10^5$	10	10
AFM#1000	4 nanowires	1	0.22	1000	0.001	$2.2 \cdot 10^5$	10	10
AFM#2000	4 nanowires	1	0.22	2000	0.001	$4.4 \cdot 10^5$	10	10
Square#20	4 squares	1x1	0.22	20	0.001	$4.4 \cdot 10^3$	10	10
Square#50	4 squares	1x1	0.22	50	0.001	$1.1 \cdot 10^4$	10	10

3.2 Morphology discussion

The AFM images are not so easy to interpret due to many possible artifacts as well as surface contamination, electrostatic forces, and heterogeneous surfaces that can impact the action of the probe[39-41]. The images had to be flattened and corrected with step line correction due to line artifacts mainly produced by the parallel scanning to the nanowires. To study the evolution of geometry of the deposits with different deposition parameters such as the number of loops, we have analyzed the mean height profile of several arrays composed of four nominally-identical nanowires. Each array was fabricated under a different number of loops. All the images were equally treated with Gwyddion imaging software.
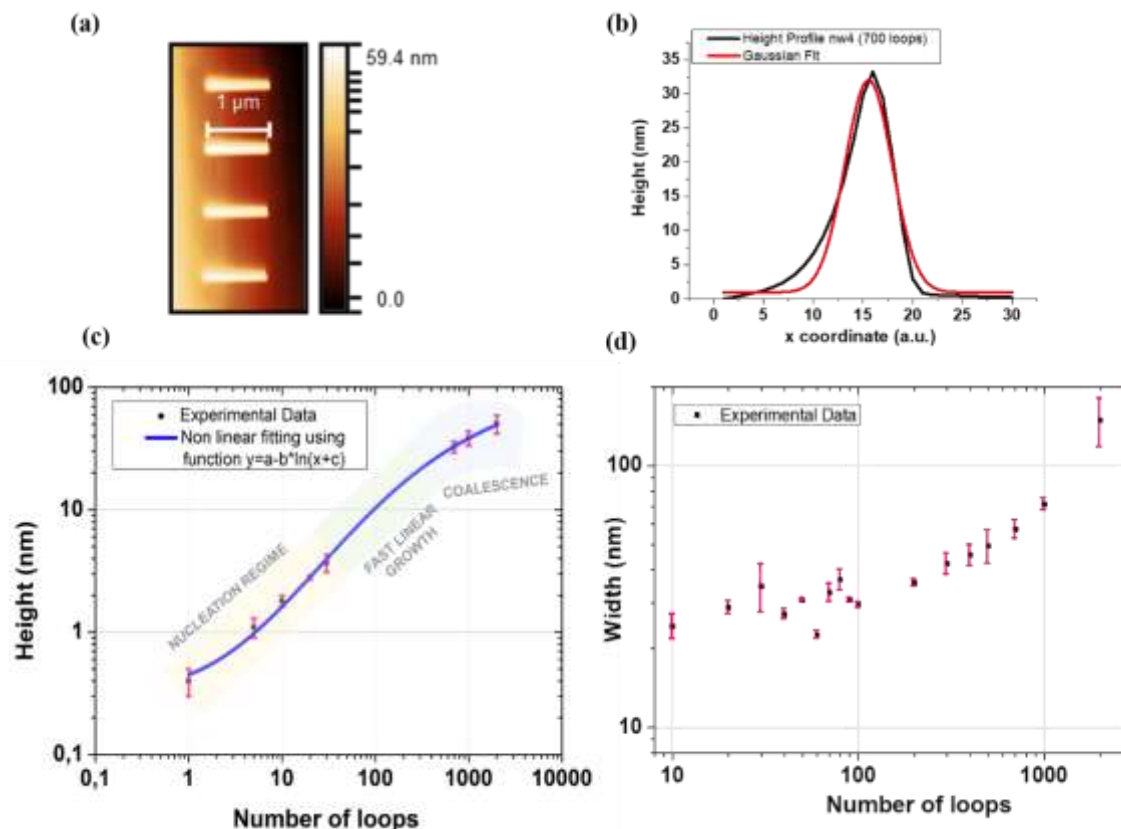
Figure 7. (a) AFM image of sample AFM#700 obtained in contact mode. This is an array of 4 nanowires 1 µm length fabricated with 0.22 nA, 1µs dwell-time and 700 loops.
(b) Height profile of a nanowire of AFM#700 sample. Experimental data (black line) and Gaussian fitting (red line) show the mean height of this array ~32.7 nm
(c) Height versus the number of loops (axis on logarithm scale). Logarithm fitting (blue line). Error bars (red color) show the standard deviation (σ) of the measurements.
(d)Width versus the number of loops (axis on logarithm scale). Error bars (red color) show the standard deviation (σ) of the measurements.

As we can observe in **Figure 7**(c) there is a fast growth of the height with a lower number of loops but when the number of loops increases the slope of the curve decreases. This provides us very useful information not only to take control over geometry with more precision and also to obtain empirical recipes but it also allows us to study different steps in the nanowire fabrication process such as the nucleation, followed by growth and coalescence of the material[54,55]. The information we can extract from the figure is that there is linear growth above 30 and below 300

loops approximately. The observed uniformity seems to indicate that there is no presence of anomalous halo produced by the SEs[23]. The results of our measurements are shown in Table 3.

Table 3. Height profile measurements mean values and standard deviation (σ) for arrays of nanowires from AFM#1 to AFM#2000.

Sample	AFM #1	AFM #5	AFM #10	AFM #20	AFM #30	AFM #700	AFM #1000	AFM #2000
Loops	1	5	10	20	30	700	1000	2000
Height (nm)	0.4	1.1	1.8	2.8	3.7	32.7	38.5	50.4
σ(nm)	0.1	0.2	0.2	0.1	0.6	3.5	5.2	8.5

The AFM is a standard technique to determine the height of grown deposits[32]. Information provided by previous research showed that the shape of the deposits changes with growth, as well as the size of the interaction volume of the secondary electrons[26]. As we saw in the previous section, the electron flow in this technique incorporates the contribution of secondary electrons[32], which have been seen to play a dominant role in the dissociation process[35]. The radial distribution density and lateral range of these electrons are what mainly limits this technique. Furthermore, an insulating sample can be charged if more or fewer electrons are injected as PEs than SEs are emitted depending on the balance between them[26]. This situation creates an electric field that could ionize or polarize the precursor molecules and drive them towards the irradiated spot[26].

Some models where possible interactions between adsorbed molecules are rejected indicate that the growth rate is a function of dwell time[32]. In similar studies using the precursor $W(CO)_6$ it has been observed that if the residence time on the deposit was longer than on the substrate this resulted in a higher probability of dissociation and a higher growth rate once the deposit had formed[35]. The longer the residence time, the greater the probability of dissociation[23]. The growth process depends on the adsorbed molecules and the growth speed depends in turn on the residence time of the same[23]. Likewise, a higher growth speed could prevent the incorporation in the deposits of contaminant species[23]. The opposite situation has been observed previous experimental research in which nanodeposits of W superconductors grown by a focused ion beam where the growth rate of W on SiO_2 was much higher than the growth rate on the already grown substrate[23]. The growth of W per ion beam began with the nucleation of W particles when a low ion dose was used[23]. As the dose increases, the particles grow until they melt, creating a continuous film. Here it was observed that once the continuous film was formed, the growth was linear concerning the dose of electrons used[23].

Comparing with our experimental data we could affirm that the rapid slope of the initial curve could indicate that the residence time is also greater on the first nucleated deposits than on the Si substrate. It must be taken into account that as soon as the growth process begins, the surface goes from being the substrate to being the deposit[23]. As we can see in **Figure 7**(c), the relation between the height and the number of loops is not linear and there is a logarithm trend. If we represent the graphic on a logarithm scale we can see a sigmoidal curve that is normally observed in sigmoidal growth kinetics[54,55]. In our case, in these samples, the difference is only the number of loops. So the greater the number of loops, the higher is the total time and the dose of electrons. However, as our fabrication approach is pulsed in our case it is different because the loops are between the lines. That's why we have shorter dwells compared to literature. We go from one end of the thread to the

other. Then we go to the extreme, stop for 50ms, and start the next loop. What we can say is that there is an initial induction period that is attributed to the nucleation regime and when the stable nuclei are formed there is a fast linear growth period and finally the growth slows down[54,55]. Nucleation, growth and coalescence are processes that depend in turn on many factors such as the residence time. As we commented before, this parameter varies continuously since the surface is being continuously modified during this process. Additionally, the secondary electron yield is different on the SiO_x surface than when there is metal deposited. The presence of a certain amount of deposited metal may influence the amount of precursor decomposed.

In similar studies, it has been pointed out that if the size of the deposit is small enough, the amount of material deposited is not linearly proportional to the time during which they are exposed to the electron beam but is determined by the statistics of the dissociated molecules[35]. The presence of charging effects might be possible after reaching a determined height and receiving a determined electron dose. This could spread the focus of the e-beam, or induce a lower dissociation of $W(CO)_6$ and hence a slower growth. It must be taken into account that the growth process through FEBID is produced by a set of complex physical phenomena influenced by a high number of factors such as electron density and radial energy distribution, residence time, or the heating produced by the beam[23].

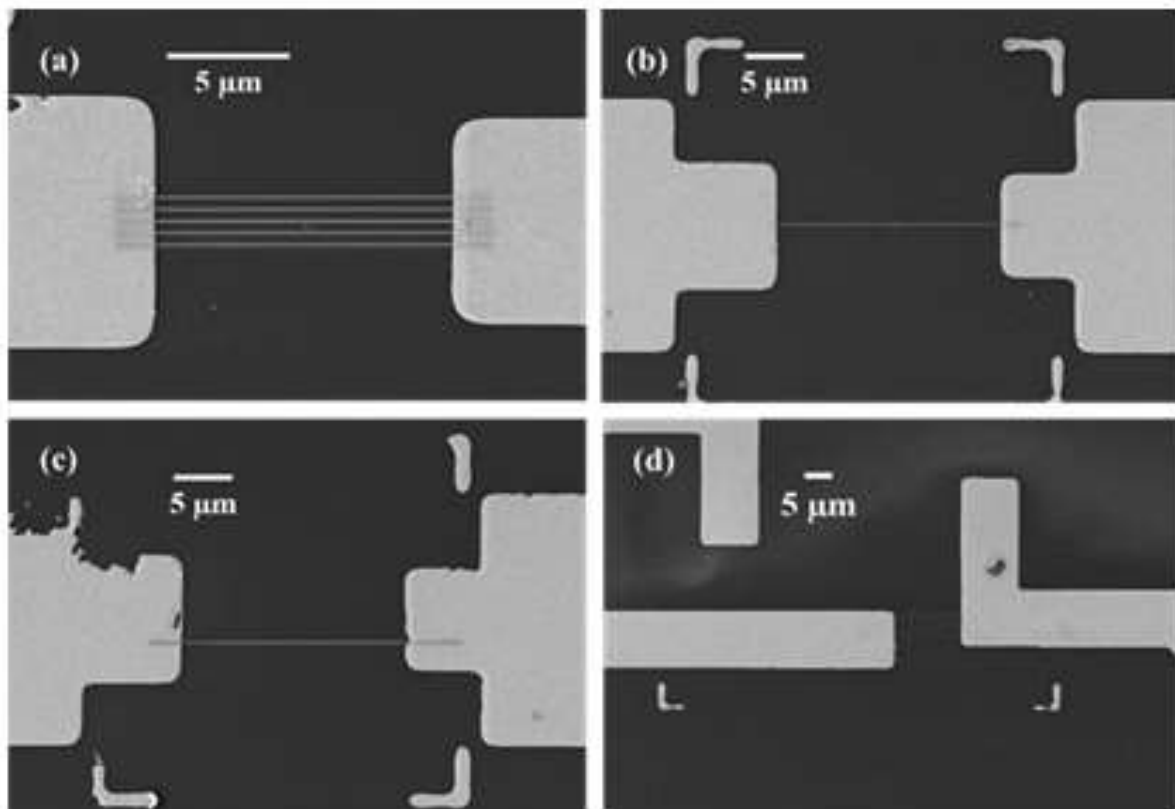**Figure 8**. SEM images. (a) Sample A_0: Five 15 µm-long nanowires fabricated using a dwell-time of 0.1 ms and 50 loops. (b) Sample A_1: A 20 µm-long nanowire fabricated using a dwell-time of 0.1 ms and 50 loops. (c) Sample B_0: A 25 µm-long nanowire fabricated using a dwell-time of 0.1 ms and 50 loops. (d) Sample B_{2D}: Five 25 µm-long nanowires using a dwell-time of 0.001 ms and 2500 loops.

Despite using an amorphous SiO_x substrate[35], SEM images obtained in situ during fabrication show very narrow nanowires (**Figure 8**). The mean width varied between 38 nm and 64 nm depending on the deposition parameters. We also observe a general trend for the creation of wider deposits when the exposure time is increased due to a higher dose of electrons[35]. The information provided by the SEM images about the width and the height information provided by AFM permits us to make sure that high-aspect ratios can be achieved. Furthermore, the possibility of high reproducibility in the growth of these nanowires would be a great advantage, since, as other groups have done, this would allow obtaining samples with very similar transport properties[32].

3.3 Composition discussion

The results of Raman spectroscopy allow us to correlate the deposition parameters, the microscopic configuration of C clusters present, as well as the physical properties[29]. In WC sheets grown by CVD or physical vapor deposition (PVD), compositional analysis indicates the presence of a mixture of different phases of tungsten carbide and oxides of different stoichiometries[56]. The material grown in FEBID is normally composed of the metallic element, C, and O that comes from the precursor or contaminants (oxygen, hydrocarbons, and water vapor)[23] as previously shown in **Figure 3**. The microstructure of materials obtained by FEBID can be amorphous, nanogranular/nanocomposite, or nanocrystalline[32]. Among the amorphous and polycrystalline structures are nanogranular systems that consist of nano-crystallites embedded in a matrix rich in C[32]. Depending on the microstructure, the physical properties vary substantially[32].
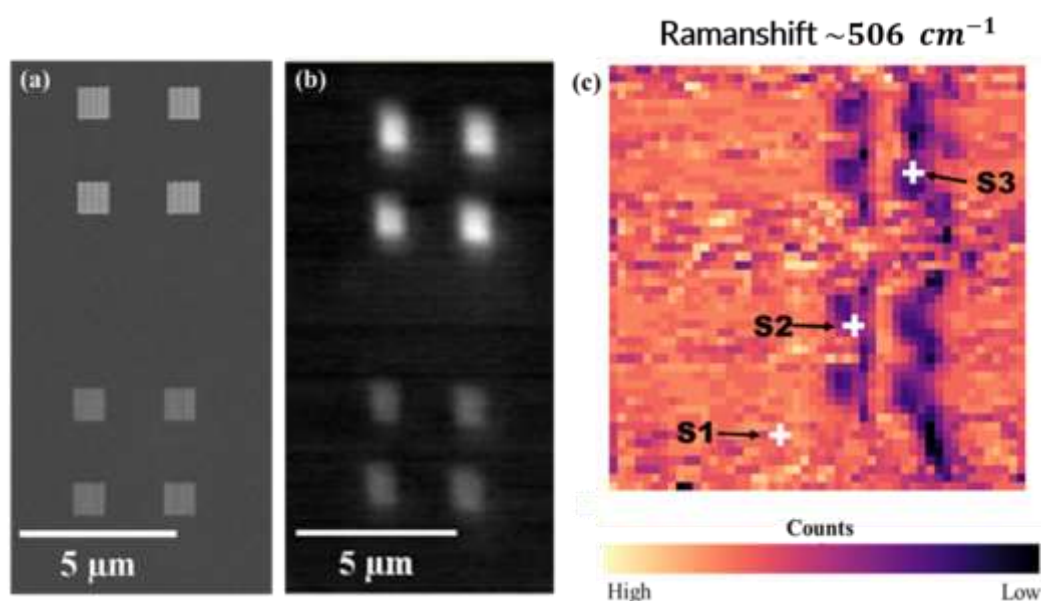
Figure 9. Square#50 and Square#20 samples 1 µm length fabricated with a beam current of 0.22 nA, dwell-time of 0.001 ms, 50 and 20 loops respectively. (a) SEM images (b) Reflectance map provided by the photodiode. (c) Raman map at 506 cm^{-1} Raman shift (1st order of Si peak). The map is 15 x 15 µm. Spectra of points *S1*, *S2* and *S3* are shown in Figure 10.

We have used samples Square#20 and Square#50 to study the composition by Raman spectroscopy. Each of them consists of a set of 4 squares with sizes of 1 µm x 1 µm (**Figure 9**(a)). We also carried out this technique over an array of nanowires. However, the peaks there could not be clearly distinguished as the brightness of the electrodes masks the Raman map and may reflect

15

a lot from the laser. Gold has a reflectivity of r ~ 0.7 around a wavelength of 550 nm[57] and in this energy range, chromium also has high reflectivity[58]. The reflectance map (**Figure 9**(b)) shows regions more reflective inside the deposits.

In the regions outside the deposits only Si Raman peaks are observed (*S1* spectra in **Figure 10**(a)). Inside them we can see more contributions (*S2* and *S3* spectra in **Figure 10**(a)). This can also be observed in **Figure 11**. Although we can see in **Figure 10**(b), both peaks D and G due to the deconvolution of the Gaussians the signal-to-noise ratio (SNR) is low .This SNR could probably be due to errors in the alignment of the laser in the optical path of our experimental set-up. In any case, the presence of both peaks is intuited. According to this research[56], the D-peak and G-peak were only present for samples with a carbon content greater than 50 % at[56]. This is an indication that the atomic composition of C in our deposits is high.
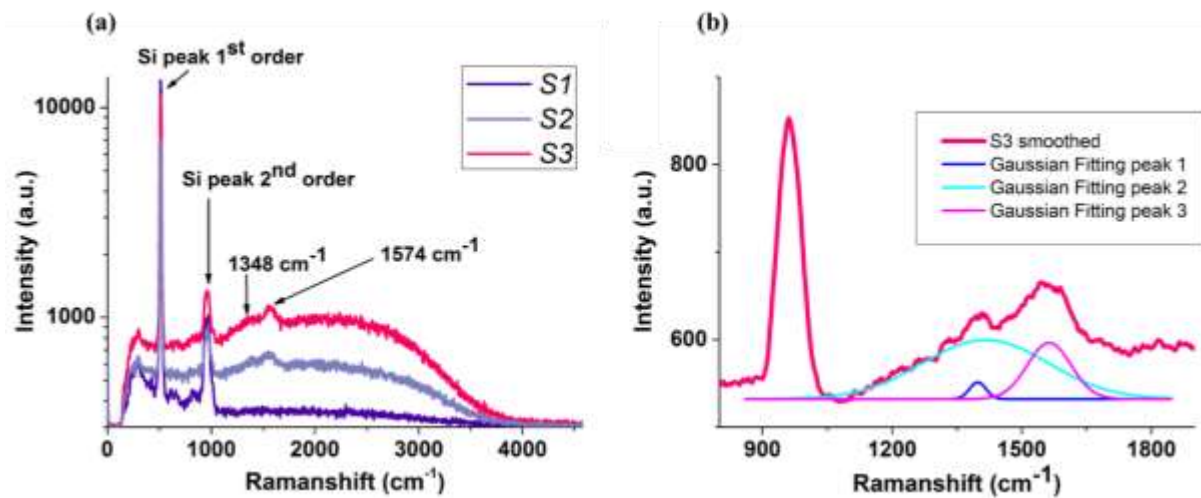
Figure 10. Square#50 and Square#20 samples (a) Raman spectra zoom of points *S*1, *S*2, and *S*3. (b) Smoothed spectra in *S*3 point and deconvolution of Gaussian peaks.

The use of Raman spectroscopy in the study of tungsten carbide nanostructures and its microstructure has already been used by other groups[26,56,59] as it is shown in Table 5. This Table 5 assembles data from several research of Raman peak positions and their associated modes. Besides, we have found in the literature that peaks at higher wavenumbers (1200-1850 cm^{-1}) could provide information on the amorphous carbon matrix[27,56] and changes in the phase of nanostructured WC sheets[56], basing on the position and full width at half maximum (FWHM) of the carbon fingerprints[29,56].

Figure 11. Square#50 and Square#20 samples

(a) Raman Map at 528 cm^{-1} Raman shift. Map is 15 x 15 μm in area.

(b) Raman spectra of colored points *1 to 5*. Region outside FEBID deposits.

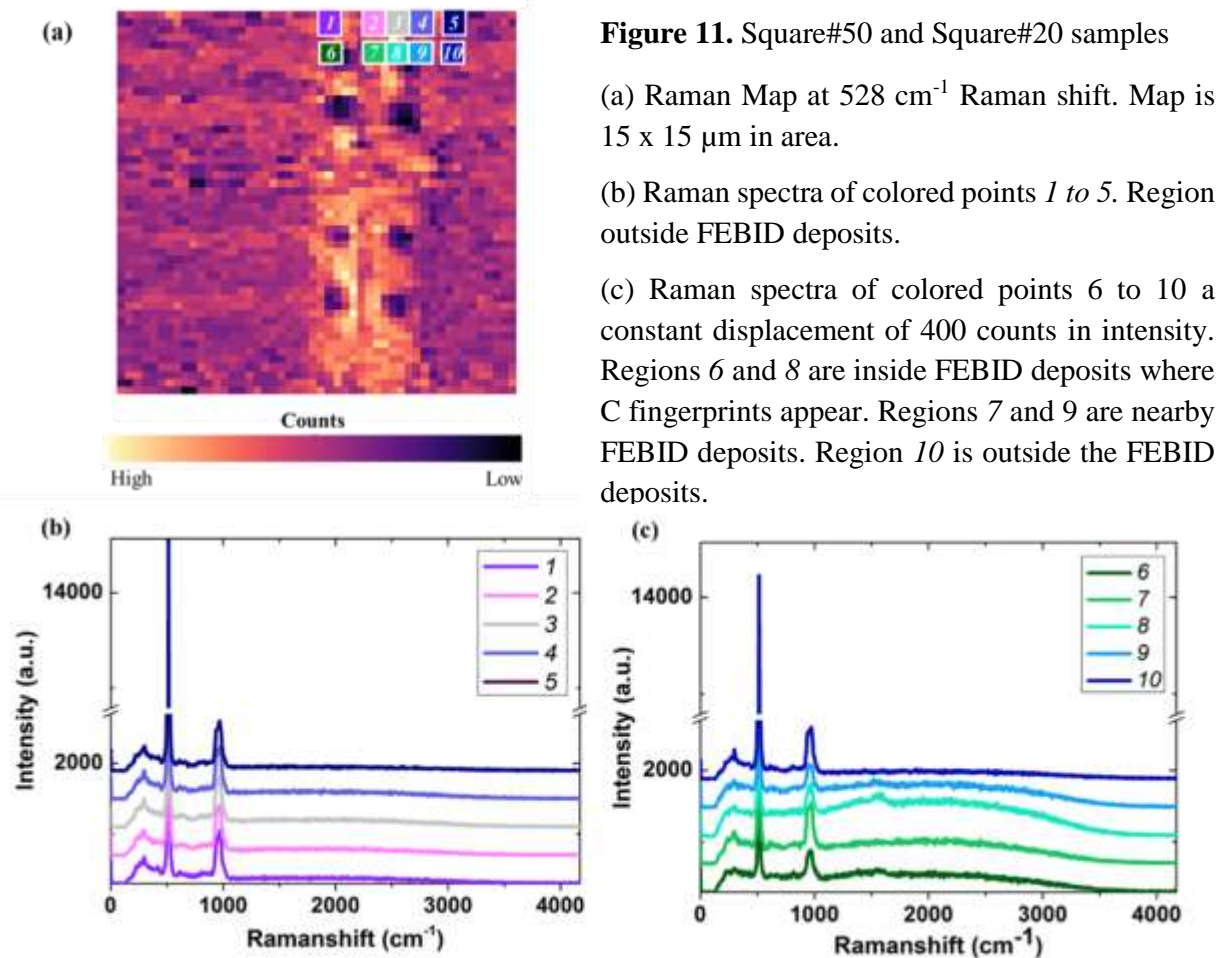(c) Raman spectra of colored points 6 to 10 a constant displacement of 400 counts in intensity. Regions *6* and *8* are inside FEBID deposits where C fingerprints appear. Regions *7* and *9* are nearby FEBID deposits. Region *10* is outside the FEBID deposits.

The analysis of different C phases by Raman spectroscopy is complex[29]. The intensity of the lines provides a measure of the relative abundance of C while the width is more related to the size of the cluster, the order within it, and its distribution[29]. The structure of the carbonaceous matrix could be determined by analyzing the positions of the D and G peaks and their ratios of relative intensities[27]. Typically, the increase in the I_D/I_G ratio implies that the number of nanocrystalline graphitic inclusions increases[29].

In the literature we have found that the narrowing of the peak D and G[56] were stated to be consistent with an increase in the matrix order of the sp$_2$ matrix -C attached[56]. The increase and sharpening of the D and G peaks correspond to a progressive crystallization of the initial phase of amorphous C towards nanocrystalline graphite[56]. This is opposite to our experimental results so it seems that there is an important contribution of amorphous C. If we compare with other research[27,56] this seems to be congruent with our experimental results. Our Raman spectroscopy measurements indicate the existence of an amorphous structure.

Furthermore, our experimental results do not show us clearly the WC peaks. Although there seems to be a peak in the low-frequency range around 200 cm^{-1} (**Figure 10**(a)), the number of counts is very small. The SNR is not high enough to be able to affirm it. It might be masked by the contribution of other different Raman peaks with higher intensity or by the reflection of the laser. Despite integrating a longer time (2 seconds per point) the SNR did not improve much more. In these circumstances, it is very difficult to determine the peaks associated with the WC or the relative intensity of the C peaks. Even though the results obtained do not allow us to identify the

WC peaks, the laser reflection together with the reflectance map seems to indicate the presence of some metallic composition within the deposits. This information will be complemented with ex-situ electrical transport measurements in the next section.

Table 5. Summary of Raman peak positions from different research.

Raman Peaks positions (cm^{-1})		*Associated mode*
690 and 860	685-805	Stretching modes WC[27,56]
803, 704 and 127		WC oxides modes[28]
200-400		O-W-O bending modes[56]
675 and 810		W-O stretching modes[56]
960		W = O modes[56]
Wide peaks in 600-900		Different phases of carbides and oxides[56]
709 and 806	272, 716 and 807	WC[30,59]
1280	1298 and 1335	D-band (sp3-hybridized diamond-like C)[27,30,59]
1343	1350	D-line[27,28,30,56]
1580	1585	G-line[27-30,56]
2300-3300 broadening		Vibrations of C-H bonds and D and G mode of the graphitic C planes in the free C[28]

Apart from problems with the alignment and focus of the laser beam, the low SNR may be due to the small width of the nanowire compared to the diameter of the laser[23]. We also have to take into account that as the compositional analysis has been carried out ex-situ, there is the possibility that the composition of the deposits has been modified by external agents[23]. Even in situ contamination of the samples is also possible since residual gas could also affect, acting as a second precursor[32].

To clarify the elemental composition, additional research is needed. If the problem with these samples is derived from the small amount of material, we could fabricate samples with a greater surface area and / or thickness. We could also integrate for a longer time during the measurements or analyze its composition using another spectroscopic technique, as have other groups such as XPS[59], energy-dispersive x-ray spectroscopy (EDX)[23,32,34], reflection absorption infrared spectroscopy (RAIRS)[34,] or high-resolution energy loss spectroscopy (HREELS)[23,34].

On the other hand, it has been found in other studies that by using spectroscopic measurements, a relationship of the composition with the time of irradiation of the electron beam and that the incident electrons could produce atomic displacements of oxygen and carbon at particular energies[31]. At higher current densities the C content in an electron beam induced deposition (EBID) reservoir frequently decreases[34]. For instance, a significant decrease in C has been seen after annealing since due to the partial pressure of oxygen it can be effused out[56]. That is, the D and G bands decrease due to the elimination of C[56] and new peaks appear at lower frequencies that indicate incipient oxidation of the WC phases mixed with the carbides[56]. It has also been seen that the lower the pitch was the more amorphous was the matrix of carbon[27]. Moreover, the dwell time can be a decisive parameter that varies the composition of the material significantly. It would be interesting for us to do more research in this direction for future experimental work.

3.4 Electrical properties discussion

The final goal of this project is the fabrication of nanowire single photon detectors based on hybrid superconducting materials so these measurements are of high relevance. In similar studies[27,31,33] it has been observed that the deposition parameters and the conditions for a given precursor have a significant effect in the microstructure of the resulting deposits. The microstructure is intrinsically related to its electrical properties. In particular, in FEBID structures using $W(CO)_6$[32], the metallic content can be modulated by electron beam parameters. Despite this, the interpretation of electrical properties is complex as changes in the content of the sample modify the microstructure itself[32]. For instance, in an array of 2D WC nanodots, it has been observed that the variation of the energy of the electron beam current or the raster constant can modulate the electrical properties[27].

From the current-voltage (I-V) curves and the dependency of the electrical conductivity with the temperature, several electrical transport mechanisms can be studied[27]. For electrical conduction, 3 regimes have been distinguished: metallic, a transition from metal to insulator, and insulator[23]. In granular metals, depending on how is the relation of the conductivity and the temperature, transport can be metallic, tunnel type, or it can be thermally activated associated with variable-range-hopping (VRH)[23,32] with an Arrhenius type conductivity and a large energy gap in agreement with an insulating regime[23,32]. In granular metals, the electrical transport properties depend on the tunnel conductance between neighboring grains and the fluctuations of chemical potentials between grains due to charged impurities in the matrix[32]. As a consequence, they can have a metallic, partial-insulating or insulating behavior[32].

In Pt-C FEBID structures it has been found that it is possible to modulate the system through the metal-insulator transition by irradiating the post-growth deposits[32]. The four orders of magnitude increase in conductivity were identified as being due to a change in structure from an amorphous C to nanocrystalline graphite[32]. In similar studies using the precursor $W(CO)_6$[32] it has been observed that this transition could be controlled by the beam step size. In this research[27] the nanostructures with the highest pitch were in the insulator region and the samples with the lowest pitch were in the metallic region[27]. In this case, the deposits were homogeneous enough so that the Gaussian profile of SE could overlap[27]. For large pitches, they found an Arrhenius-like behavior[32].

The electrical resistivity (ρ) in samples manufactured by FEBID has been found to depend strongly on the metallic content in the microwires[23]. Different research has shown ρ at RT in nanowires of Fe with values from 186 $\mu\Omega\cdot$cm to $3,84.10^5$ $\mu\Omega\cdot$cm as a function of Fe content[23]. Values of $\rho > 10^3$ $\mu\Omega\cdot$cm are far from the metallic conduction regime and values from $\rho > 10^4$ $\mu\Omega\cdot$cm at RT usually indicates insulating behavior[23].

We measured samples A_0, A_1, B_0 and B_{2D} in the probe station by two probe method. Their size and deposition parameters are specified in Table 2 and *Figure 8*. The electrical resistance of nanowires is expressed as $R=\rho_{1D}L$, where L is the length of the wire. In those samples formed by arrays of parallel nanowires (samples A_0 and B_{2D}) instead of a single nanowire, the resistance of the nanowire was obtained from the calculation of equivalent resistance of all the nanowires in parallel. We can see these results in Table 6.

Table 6. Electrical resistance and resistivity values measured from samples A_0, A_1, B_0 and B_{2D} at RT by two-probe method.

SAMPLE	Electrical resistance (Ω)	$\rho_{1D}(\Omega.cm)$
A_0	$1.10 \cdot 10^5$ (total array)	$3.70 \cdot 10^8$
	$5.60 \cdot 10^5$ (one nanowire)	
A_1	$1.25 \cdot 10^6$	$6.24 \cdot 10^8$
B_0	$7.50 \cdot 10^6$	$3.0 \cdot 10^9$
B_{2D}	$5.8 \cdot 10^4$ (total array)	$1.15 \cdot 10^8$
	$2.89 \cdot 10^5$ (one nanowire)	

The resistivity results at RT for samples A_0 and A_1 were $3.7 \cdot 10^8$ Ω·cm and $6.24 \cdot 10^8$ Ω·cm, respectively. These are values much higher than those found by other groups ($\rho = 2500$ $\mu\Omega$·cm) but they used a dose of electrons greater than ours[31]. In this other study making reference to other research they reported nanowires fabricated by electron beam induced CVD (EBICVD) using $W(CO)_6$ as a precursor with a resistivity of 600-200,000 $\mu\Omega$·cm at RT[31]. Analyzing our samples B_0 and B_{2D}, although the dose of electrons is lower in B_{2D} than in B_0, the shortening of the dwell-time and the increase in the number of loops provide a higher conductivity value for B_{2D}. Sample B_0 fabricated with the same deposition parameters as A_0 and A_1 but with twice the diameter but longer, has a higher resistivity than A_0 and A_1. In any case, all these values are in the limit between insulating and semiconductor materials.

A possible explanation for our high resistance value in addition to the contact resistance could be due to the existence of a possible lower W content and higher C content and / or due to an amorphous structure. Due to the scattering of electrons in amorphous materials, the free path electron medium is greatly reduced[23]. This could also be responsible for an increase in Tc, as it seems to indicate in amorphous nanodeposits of W grown by FIBID[23]. Furthermore, in FEBID it has been observed that organometallic precursors tend to form mainly amorphous deposits[32]. It is important to take this into account because it has been proven that above a certain impurity concentration the material could not become superconducting at low temperature (LT)[31].

Moreover, in **Figure 12**(a) we can see that at low range voltage sweep there is ohmic behavior but at high voltage, there is a bending typically related to tunneling electric transport[60,61,62] (**Figure 12**(b-e)). This is congruent with the high resistivity values, as well as the big contribution of amorphous carbon observed in Raman measurements.

The amorphousness of our samples should be corroborated by transmission electron microscopy (TEM) measurements, although the thickness of the samples should be less than 100 nm[23]. It might be possible to modify this amorphous structure through post-irradiation treatments as has been demonstrated in Co-Pt[32]. Much research is still needed in this field as beam-induced chemistry is still neither well understood nor well-controlled[31]. Beam-induced chemical reaction pathways are very complex[32].

Before making a definite statement additional work is needed. To check if they have a metallic behavior, we would have to study the evolution of I-V curves as we decrease the T. In FEBID metallic structures using $W(CO)_6$ is expected a good conductivity with increasing values if the temperature is lowered[33]. Performing four-probe electrical measurements under cryogenic conditions are expected.
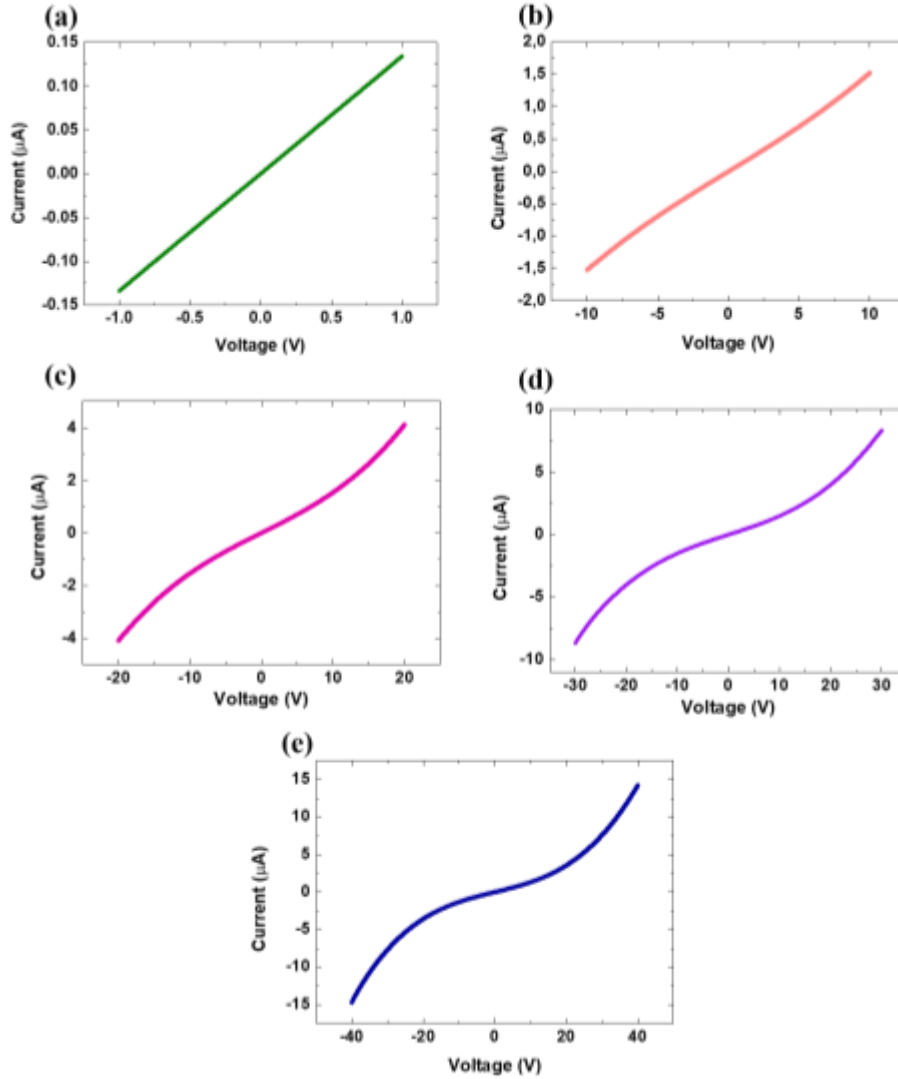
Figure 12. I-V curves of sample B_0 at a different range of sweep voltage.

4. Conclusions and remarks

Nanowires with high aspect-ratio have been fabricated by PFEBID as it is corroborated by both SEM and AFM images. Likewise, the fabrication of nanowire arrays shows that using this technique it is possible to manufacture structures with a meander-shaped geometry, as has been carried out in other research on SNSPD but with the EBL technique[1,4,5,18,19]. The relation between the height and the number of loops is not linear and this allows the creation of empirical recipes with better control on the nanofabrication process. Additionally, the nanowires with equal deposition parameters show a good logarithmic fit that is included within the uncertainty interval defined by their standard deviation of height. This seems to indicate that this technique provides a reliable way of fabrication nanowires not only in their width and length but also in their thickness.

Regarding its composition and microstructure, the experimental results obtained by Raman spectroscopy do not show clearly the peaks associated with tungsten carbide. This may be due to masking by the contribution of other peaks with higher intensity, to background noise, or laser reflection by the deposits themselves. However, Raman peaks D and G corresponding to

amorphous carbon are intuited in the region of the deposits. The G peak is clearly present. The presence of amorphous carbon would be congruent with similar studies from other groups using FEBID. Nevertheless, additional research is required to clarify the elemental composition. It might be necessary to perform different spectroscopic techniques such as EDX.

Furthermore, electrical measurements show the ohmic behavior of the nanowires at RT. The resistivity values vary from $1.15 \cdot 10^8$ $\Omega \cdot$cm to 3.10^9 $\Omega \cdot$cm depending on the deposition parameters. Its correlation matrix is shown in **Figure 13**. These values are several orders of magnitude higher than others found by other groups employing FEBID[31]. The possible lower tungsten content could explain the higher resistivity and this would be consistent with the literature since we have used a much lower total dose of electrons. The contact resistance has not been taken into account in the calculation of the electrical resistance of the nanowires and it is known that their influence in one-dimensional materials is extremely important. Besides, the possible presence of organic contaminants in the region contacted with the electrodes could also affect. These results indicate that there is probably a semiconductor or insulating material, however, to check if there is metallic behavior or a superconducting transition it needs to be measured at low temperature. Further electrical measurements at low temperatures inside the cryostat are expected.
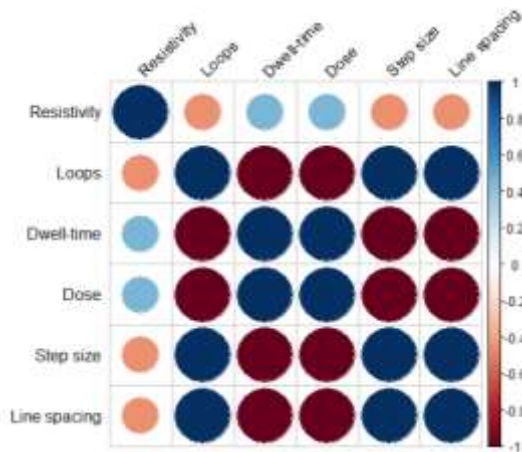

Figure 13. Correlation matrix between resistivity and deposition parameters.
The intensity and size of the circle are proportional to the correlation factor.
The larger the circle, the greater the correlation between variables. The blue color indicates a positive correlation. The red color indicates a negative correlation.

A deeper understanding is required at the molecular level of the interactions between the substrate, the electrons, the adsorbed precursor molecules[34], as well as the accompanying bond break events and the deposition process[32]. It would also be interesting to investigate how to provide a suitable chemical environment to fabricate optimized deposits by this technique[32]. One could also study the effect of some heat treatment for purification. Further optimization of the nanofabrication process will be performed to improve the metal content. Future research related to their photo responsivity is also expected.

References

1. Hadfield, R. H. Single-photon detectors for optical quantum information applications. *Nat. Photonics* **3**, 696–705 (2009).

2. Yamashita, T. et al. Origin of intrinsic dark count in superconducting nanowire single-photon detectors. Appl. Phys. Lett. 99, 2011–2014 (2011).

3. Burenkov, V., Xu, H., Qi, B., Hadfield, R. H. & Lo, H. K. Investigations of afterpulsing and detection efficiency recovery in superconducting nanowire single-photon detectors. J. Appl. Phys. 113, (2013).

4. Atikian, H. A. et al. Superconducting nanowire single photon detector on diamond. Appl. Phys. Lett. 104, 1–5 (2014).

5. Pernice, Wolfram HP et al. Superconducting Devices in Quantum Optics. Quantum Science and Technology; Springer, 2016, Chapter 4: Waveguide Integrated Superconducting Nanowire Single Photon Detectors on Silicon;p.85-105

6. Najafi, Faraz et al. Superconducting Devices in Quantum Optics. Quantum Science and Technology; Springer, 2016, Chapter 1:Superconducting Nanowire Architectures for Single Photon Detection : p.3-30

7. Gondek. Optical optimization of organic solar cell with BH. Opto-Electronics Rev. 22, 77–85 (2010).

8. Zhang, W. J. et al. NbN superconducting nanowire single photon detector with efficiency over 90% at 1550 nm wavelength operational at compact cryocooler temperature. Sci. China Physics, Mech. Astron. 60, (2017).

9. Guillamón, I. et al. Nanoscale superconducting properties of amorphous W-based deposits grown with a focused-ion-beam. New J. Phys. 10, (2008).

10. Koppens, F. H. L. et al. Photodetectors based on graphene, other two-dimensional materials and hybrid systems. Nature Nanotechnology vol. 9 780–793 (2014).

11. Natarajan, C. M., Tanner, M. G. & Hadfield, R. H. Superconducting nanowire single-photon detectors: Physics and applications. *Supercond. Sci. Technol.* **25**, (2012).

12. Cheung, J., Migdall, A. & Castelletto, S. Journal of Modern Optics: Introduction. J. Mod. Opt. 54, 137–139 (2007).

13. Gerrits, Thomas et al. Superconducting Devices in Quantum Optics. Quantum Science and Technology; Springer, 2016, Chapter 2: Superconducting Transition Edge Sensors for Quantum Optics: p.31-60

14. Stevens, M. J. et al. Fast lifetime measurements of infrared emitters using a low-jitter superconducting single-photon detector. Appl. Phys. Lett. 89, 1–4 (2006).

15. Sensibilidad espectral. HiSoUR Arte Cultura Historia (2020). at <https://www.hisour.com/es/spectral-sensitivity 27054/#:~:text=La%20sensibilidad%20espectral%20es%20la,de%20onda%20de%20la%20se%C3%B1al.>

16. Schrieffer, J. R. Theory of super conductivity. Theory Supercond. 1–332 (2018) DOI:10.1201/9780429495700.

17. Ivry, Y. *et al.* Superconductor-superconductor bilayers for enhancing single-photon detection. *Nanotechnology* **28**, (2017).

18. Verma, V. B. et al. Superconducting nanowire single photon detectors fabricated from an amorphous Mo0.75Ge0.25 thin film. Appl. Phys. Lett. 105, 0–5 (2014).

19. Dorenbos, S. N. et al. Low noise superconducting single photon detectors on silicon. Appl. Phys. Lett. 93, (2008).

20. Constancias, C., Espiau de Lamaëstre, R., Louveau, O., Cavalier, P. & Villégier, J.-C. Patterning issues in superconducting nanowire single photon detector fabrication. J. Vac. Sci. Technol. B Microelectron. Nanom. Struct. 25, 2041 (2007).

21. Kavitha, M., Sudha Priyanga, G., Rajeswarapalanichamy, R. & Iyakutti, K. First principles study of the structural, electronic, mechanical and superconducting properties of WX (X=C, N). J. Phys. Chem. Solids 77, 38–49 (2015).

22. Willens, R. H. & Buehler, E. The superconductivity of the monocarbides of tungsten and molybdenum. Appl. Phys. Lett. 7, 25–26 (1965).

23. Córdoba Castillo, R. *Nanoestructuras funcionales fabricadas mediante un haz de electrones o iones focalizado. Nanoestructuras funcionales fabricadas mediante un haz de electrones o iones focalizado* (2012). doi:10.26754/uz.978-84-15770-08-4.

24. Mattioli, F. et al. Electrical characterization of superconducting single-photon detectors. J. Appl. Phys. 101, 1–6 (2007).

25. Hadfield, R. H. et al. Single photon source characterization with a superconducting single photon detector. Opt. InfoBase Conf. Pap. 13, 6746–6753 (2006).

26. de Boer, S. K., van Dorp, W. F. & De Hosson, J. T. M. Charging effects during focused electron beam induced deposition of silicon oxide. *J. Vac. Sci. Technol. B, Nanotechnol. Microelectron. Mater. Process. Meas. Phenom.* **29**, 06FD01 (2011).

27. Porrati, F. et al. Artificial granularity in two-dimensional arrays of nanodots fabricated by focused-electron-beam-induced deposition. Nanotechnology 21, (2010).

28. Krasil'nikov, V. N., Polyakov, E. V., Khlebnikov, N., Tarakina, N. V. & Kuznetsov, M. V. Precursor synthesis and properties of nanodispersed tungsten carbide and nanocomposites WC:nC. Ceram. Int. 43, 4131–4138 (2017).

29. Radić, N., Pivac, B., Meinardi, F. & Koch, T. Raman study of carbon clusters in W-C thin films. Mater. Sci. Eng. A 396, 290–295 (2005).

30. Gabhale, B. et al. High band gap nanocrystalline tungsten carbide (nc-WC) thin films grown by hot wire chemical vapor deposition (HW-CVD) method. J. Nano- Electron. Phys. 10, 1–6 (2018).

31. Luxmoore, I. J. *et al.* Low temperature electrical characterisation of tungsten nano-wires fabricated by electron and ion beam induced chemical vapour deposition. *Thin Solid Films* **515**, 6791–6797 (2007).

32. Huth, M. *et al.* Focused electron beam induced deposition: A perspective. *Beilstein J. Nanotechnol.* **3**, 597–619 (2012).

33. Huth, M., Porrati, F. & Dobrovolskiy, O. V. Focused electron beam induced deposition meets materials science. *Microelectron. Eng.* **185**–**186**, 9–28 (2018).

34. Wnuk, J. D. *et al.* Electron beam deposition for nanofabrication: Insights from surface science. *Surf. Sci.* **605**, 257–266 (2011).

35. Van Dorp, W. F. et al. Molecule-by-molecule writing using a focused electron beam. ACS Nano 6, 10076–10081 (2012).

36. Van Dorp, W. F. The role of electron scattering in electron-induced surface chemistry. *Phys. Chem. Chem. Phys.* **14**, 16753–16759 (2012).

37. Rosenberg, S. G., Barclay, M. & Fairbrother, D. H. Electron induced reactions of surface adsorbed tungsten hexacarbonyl (W(CO)6). *Phys. Chem. Chem. Phys.* **15**, 4002–4015 (2013).

38. Hydrocarbon contamination control for electron microscopes, such as TEM, SEM and FIB. Piescientific.com (2020). at <https://www.piescientific.com/Application_pages/Applications_Analytical_SEM>

39. Hornyak, G., Dutta, J., Moore, J. and Tibbals, H., 2008. *Introduction To Nanoscience And Nanotechnology*. 1st ed. CRC Press.

40. Uchihashi, T. & Toshio, A. High-speed AFM and biomolecular processes. At. Force Microsc. its use Biomed. Res. 736, 285–300 (2011).

41. Haugstad, G., 2012. *Atomic Force Microscopy*. Hoboken, N.J.: Wiley.

42. Camarero, M. Molecular Nanoscience and Nanotechnology Optical characterization of few-layer MoS 2 mechanical resonators Master Thesis. Course 2018-2019 Víctor Marzoa

Camarero.

43. NTEGRA – Modular SPM (AFM, STM) system | NT-MDT SI. Ntmdt-si.com (2020). at <https://www.ntmdt-si.com/products/modular-afm/ntegra-ii>

44. New model of Etalon probes for both contact and amplitude modulation modes. Ntmdt-si.com (2020). at <https://www.ntmdt-si.com/about/news/new-model-of-etalon-probes>

45. Reimer, L., Hawkes, P., Schawlow, A., Shimoda, K. and Siegman, A., 2013. *Scanning Electron Microscopy*. Berlin, Heidelberg: Springer Berlin / Heidelberg.

46. Rostron, P., Gaber, S. & Gaber, D. Raman Spectroscopy, Review.International Journal of Engineering and Technical Research. **6**, 50-64. (2016).

47. Manual, U. attoDRY800 Cryo-Optical Table.

48. Software, D. & Phone, M. G. User Manual attocube systems ' Piezo Motion Controller. 1–81 (2018).

49. Rgb, K. & Germany, D. M. User Manual Piezo Positioning Electronic. *Attocube* 1–43 (2011).

50. Weg, E. & München, D. H. System Specifications & Test Certificate LT-APO shroud + RT-SWD shroud.

51. SemrockPartNumber:LPD02488RU.Semrock.com(2020).At<http://www.semrock.com/Filter Details.aspx?id=LPD02-488RU-25>

52. Semrock - Part Number: LP02-488RU. Semrock.com (2020). at <http://www.semrock.com/FilterDetails.aspx?id=LP02-488RU-25>

53. Jiménez Urbanos,F. Thesis, D. New Nanofabrication Routes to Tailor the Electronic Properties of MoS 2 Devices : From Field Effect Transistors to Lateral Homo- structures. (2019).

54. Thanh, N. T. K., Maclean, N. & Mahiddine, S. Mechanisms of nucleation and growth of nanoparticles in solution. *Chem. Rev.* **114**, 7610–7630 (2014).

55. Wang, F., Richards, V. N., Shields, S. P. & Buhro, W. E. Kinetics and mechanisms of aggregative nanocrystal growth. *Chem. Mater.* **26**, 5–21 (2014).

56. El Mrabet, S., Abad, M. D., López-Cartes, C., Martínez-Martínez, D. & Sánchez-López, J. C. Thermal evolution of WC/C nanostructured coatings by raman and in situ XRD analysis. *Plasma Process. Polym.* **6**, 444–449 (2009).

57. Baranowski, J. M., Grynberg, M. & Magerramov, E. M. The optical properties of GaAs:Co. Phys. Status Solidi 50, 433–437 (1972).

58. Lind, M. A. The infrared reflectivity of chromium and chromium-aluminum alloys. (1972).

59. Cheong, Y. K. et al. Characterisation of the chemical composition and structural features of novel antimicrobial nanoparticles. Nanomaterials 7, 1–16 (2017).

60. Mironov, V. L. Fundamentals of Scanning Probe Microscopy, The Textbook for Students of the Senior Courses of Higher Educational Institutions, The Russian Academy of Sciences. *Nizhniy Novgorod* (2004).

61. Jaklevic, R. C., Lambe, J., Silver, A. H. & Mercereau, J. E. Quantum interference effects in Josephson tunneling. *Phys. Rev. Lett.* **12**, 159–160 (1964).

62. Valdeś, J. & Choleva, E. Possible evidence of single electron tunneling with the scanning tunneling microscope at room temperature. *J. Vac. Sci. Technol. A Vacuum, Surfaces, Film.* **8**, 598–602 (1990).